Formation mechanism of ⟨111⟩ interstitial dislocation loops from irradiation-induced C15 clusters in tungsten

Lixia Liu,[1] Ning Gao,[2] Yangchun Chen,[3] Rongyang Qiu,[3] Wangyu Hu,[1,*] Fei Gao [4] and Huiqiu Deng [3,†]

[1]*College of Materials Science and Engineering, Hunan University, Changsha 410082, China*

[2]*Institute of Frontier and Interdisciplinarity Science, and Key Laboratory of Particle Physics and Particle Irradiation (MOE), Shandong University, Qingdao, Shandong 266237, China*

[3]*School of Physics and Electronics, Hunan University, Changsha 410082, China*

[4]*Department of Nuclear Engineering and Radiological Sciences, University of Michigan, Ann Arbor, Michigan 48109, USA*

In this paper, we report a formation mechanism of $1/2\langle 111 \rangle$ interstitial dislocation loops via the collapse of C15 clusters in bulk tungsten. The interstitial atoms formed C15 clusters in only a few picoseconds within a displacement cascade, and the transformation from C15 clusters to ⟨111⟩ interstitial loops was observed in both classical molecular dynamics and accelerated molecular dynamics simulations. This transformation was further confirmed under compressive stress, and it was determined to be accelerated once the ⟨111⟩ loops reacted with the C15 clusters. Three possible transformation processes were proposed, namely the C15 cluster directly transforming to ⟨111⟩ loops/clusters, a partial transformation to a ⟨111⟩ cluster with high mobility, thus leaving a shrunken C15 cluster behind, and a partially transformed ⟨111⟩ cluster but pinned by the adjacent shrunken C15 cluster. The formation mechanism provides an essential reference for predicting the evolution of microstructures in tungsten-based materials under irradiation.

I. INTRODUCTION

Point defects and defect clusters are formed in crystalline materials under irradiation by high-energy neutrons or ions, as indicated by various experiments and molecular dynamics (MD) simulations [1–7]. The observation of self-interstitial atom (SIA) clustering in metals via transmission electron microscopy (TEM) techniques reveals that the clusters are only nanometer-sized planar loops [4,8–10]. Several experiments have identified that these loops have a $1/2\langle 111 \rangle$ or ⟨100⟩ Burgers vector in body-centered-cubic (bcc) metals [11–15], with the exception being iron (Fe), where the ⟨100⟩ loops dominate at high temperatures [11,12]. A large proportion of radiation-induced SIAs and small SIA clusters are glissile and highly mobile [16–21], whereas they are notable components of radiation damage and play a significant role in material deterioration in terms of, for example, irradiation-induced swelling, embrittlement, hardening, and irradiation creep [22–27].

The SIA clusters formed in tungsten (W) can be presented as dislocation loops, whereas they typically contain only a few tens of SIAs, and the loop Burgers vectors are dominated by $1/2\langle 111 \rangle$ types (>75%) [13]. In recent decades, it has generally been accepted that these ⟨111⟩ interstitial loops in W were directly produced by cascade collapse [13,25]. However, due to the limitation of resolution, only the larger loops (diameter >4 nm) tended to be the focus of the TEM

analyses to maintain a consistency in terms of loop nature and Burgers vector analyses [13,14]. In fact, in the radiation damage characterization of W and W alloys implanted with 2 MeV W+ ions, the diameter of the dislocation loops in W usually did not exceed 20 nm, with the most frequent size being ⩽6 nm [14]. Yi *et al.* [13] used *in situ* electron microscopy and electron/heavy ion to study the dynamic behavior of loops, and they observed the various effects of elastic interaction among loops, including cooperative movements of two loops, which moved jointly in the same direction and eventually dragged together to form a string, and they also found that some loops may be pinned. Hu *et al.* [27] reported that, for the W samples irradiated in the High Flux Isotope Reactor (HFIR), dislocation loops and voids are the major factors contributing to the irradiation hardening at low dose levels. To date, it has been proven to be difficult for experiments to conduct direct observation of the formation processes of ⟨111⟩ interstitial loops, to understand the properties of the pinned loops, and to characterize the structure and nature of small-sized loops/SIA clusters in W. Thus, it is crucial to understand how interstitial dislocation loops are formed in irradiated W, and to explore the properties and configuration of pinned and small-sized loops/SIA clusters using simulations, since these are fundamental and important problems with clear practical consequences regarding the material properties, given that they affect the cluster mobility and kinetics of the microstructure [28,29], the dislocation-obstacle strength [30,31], and therefore the hardening, swelling, or growth of the materials [24,32]. In the present study, we report a formation mechanism of ⟨111⟩ interstitial loops via the collapse of C15 clusters, as well as exploring the nucleation and stability of C15.

---

*Corresponding author: wyuhu@hnu.edu.cn

†hqdeng@hnu.edu.cn

A primary C15 cluster exhibits a three-dimensional (3D) morphology, corresponding to 12 SIAs, which is placed at the edges of a truncated tetrahedron and surrounded by 10 vacancies, giving a total of only two additional atoms in the bcc lattice. In fact, numerous efforts have been made to better understand the C15 clusters in Fe [33–38], which presents an energetically favorable configuration according to the density functional theory (DFT) and empirical potential calculations [34], with their structural properties and dynamical stability already widely reported [35–38]. Marinica *et al.* [34] discussed systematically the mobility, nucleation, and growth mechanisms of C15 clusters in Fe. Byggmästar *et al.* [38] found that when growing C15 clusters in Fe eventually collapse, $\langle 111 \rangle$ loops are the predominant product, at least at low temperatures. Chartier *et al.* [39] reported that both $1/2\langle 111 \rangle$ and $\langle 100 \rangle$ loops can directly nucleate from C15 clusters in Fe, which was also confirmed by Zhang *et al.* [36]. However, until now there has been little information about C15 clusters in bcc W, and although the formation energy of these clusters in W, as calculated by DFT, may be higher than that of $\langle 111 \rangle$ clusters [34,40], the nucleation of C15 clusters in the primary damage state has been observed with a predominantly small size less than 2 nm, which remains immobile after the cascades but can transform into $\langle 111 \rangle$ loops/clusters during further evolutions. This may present one of the possible states of the pinned loops and small-sized clusters observed in previous experiments [13,14].

Classical MD allows for performing accurate displacement cascade simulations with picosecond timescales and for obtaining the dynamic evolution processes of atomic structures [5–7]. However, because of the timescale limitation in MD simulations, it is challenge to explore the diffusion processes with a high-energy barrier, which may occur at a timescale up to seconds or minutes. Unlike single SIAs or loops, it is impossible to simulate the diffusion of C15 clusters in W using classical MD due to its high-energy barrier, and thus it is essential to use accelerated molecular dynamics (AMD) to explore its diffusion processes. In fact, AMD has also been adopted to investigate the diffusion of $\langle 100 \rangle$ dislocation loops as well as vacancy and He-vacancy clusters in Fe [41,42]. Here, the combination of classical MD and AMD simulations provides an opportunity to explore the formation mechanism of $1/2\langle 111 \rangle$ interstitial dislocation loops in W.

In this study, we propose a formation mechanism of $1/2\langle 111 \rangle$ interstitial dislocation loops via the collapse of C15 clusters during displacement cascade processes. Here, it is observed that interstitial atoms are able to form nanosized C15 clusters with a 3D morphology in only a few picoseconds. These clusters are highly stable and can collapse into $\langle 111 \rangle$ clusters/loops at high temperatures in classical MD and AMD simulations. This transformation mechanism was also confirmed when the compressive stress field was applied, and the transformation is accelerated once the $\langle 111 \rangle$ loops react with the C15 clusters. Here, three possible transformation processes were observed: C15 clusters (i) directly collapse into the $\langle 111 \rangle$ interstitial dislocation loops, (ii) partially collapse into the $\langle 111 \rangle$ interstitial dislocation loops with high mobility, thus leaving shrunken C15 clusters behind, and (iii) partially collapse into the $\langle 111 \rangle$ interstitial dislocation loops but pinned by an adjacent shrunken C15 cluster. All of these

results indicate that the $\langle 111 \rangle$ dislocation loops can be transformed from the C15 clusters within a few picoseconds, that is, the formation of $\langle 111 \rangle$ dislocation loops may be induced by different processes in addition to the direct formation within W cascades.

II. SIMULATION METHODS AND MODEL

A. Displacement cascades with molecular dynamics simulations

The MD simulations were performed using the large-scale atomic/molecular massively parallel simulator (LAMMPS) code [43]. The Finnis-Sinclair-type interatomic potential of W developed by Chen *et al.* [44] was used for the present simulations, and the properties of the potential have been evaluated by Liu *et al.* [45,46]. This potential well reproduces the formation and migration energies of simple defects, and it correctly predicts the relative stability of radiation-induced dislocation loops with the Burgers vectors of $1/2\langle 111 \rangle$ and $\langle 100 \rangle$ in W (the $1/2\langle 111 \rangle$ loops are the most stable) [46]. It is also found that the potential is suitable for cascade simulations and the evolution of defects [45]. Here, in order to appropriately simulate the interaction of two atoms at a short distance for the cascade procedure, the Ziegler-Biersack-Littmark universal function [47] was combined with the pair interaction functions through a connection function as provided in Ref. [48]. The primary knock-on atom (PKA) recoil energies (E_{PKA}) of 20, 50, and 80 keV at 363 K were considered within $60a_0 \times 60a_0 \times 60a_0$, $100a_0 \times 100a_0 \times 100a_0$ and $120a_0 \times 120a_0 \times 120a_0$ simulation boxes, containing 432 000–3 456 000 atoms, with a_0 the lattice constant with a value of 0.316 52 nm. To avoid the channeling effect of a specific direction [49], the PKA directions were set to $\langle 135 \rangle$, $\langle 235 \rangle$, $\langle 122 \rangle$, $\langle 133 \rangle$, and $\langle 111 \rangle$, and periodic boundary conditions (PBCs) were used in all three dimensions. Before initiating the cascade, the system was equilibrated for 20 ps. Meanwhile, the time step was set to 10^{-3} ps for the relaxing processes, whereas it was automatically adapted to between 10^{-3} and 10^{-7} ps in the displacement cascade processes, with the total time for the cascade simulation varying from 30 to 60 ps, depending on the E_{PKA}. With the same routine of previous studies [1,6,7,48,49], we divided the simulation box into two parts: the interior region and the boundary region, and we applied different ensembles in the cascade processes. A Nose-Hoover [50] thermostat was applied on the outermost boundary of the box with a thickness of six atomic layers (referred to as boundary atoms) to regulate the atomic velocities based on the target temperature. The microcanonical ensemble (*NVE*) and canonical ensemble (*NVT*) were applied for the interior and boundary atoms of the simulation box, respectively. Once the displacing atoms reached the boundary layers or crossed them, the simulation would be terminated and the result would be excluded from the statistics. The point defects, such as interstitials and vacancies, were analyzed using the Wigner-Seitz cell method [1], whereas the dislocation loops were identified using the open visualization tool (OVITO) [51] and the dislocation extraction algorithm (DXA) [52]. Meanwhile, a system containing 108 040 atoms with a size of approximately $9.49 \times 21.01 \times 9.49 \ nm^3$ was used to investigate the behavior of the C15 clusters under the stress field, with the PBCs
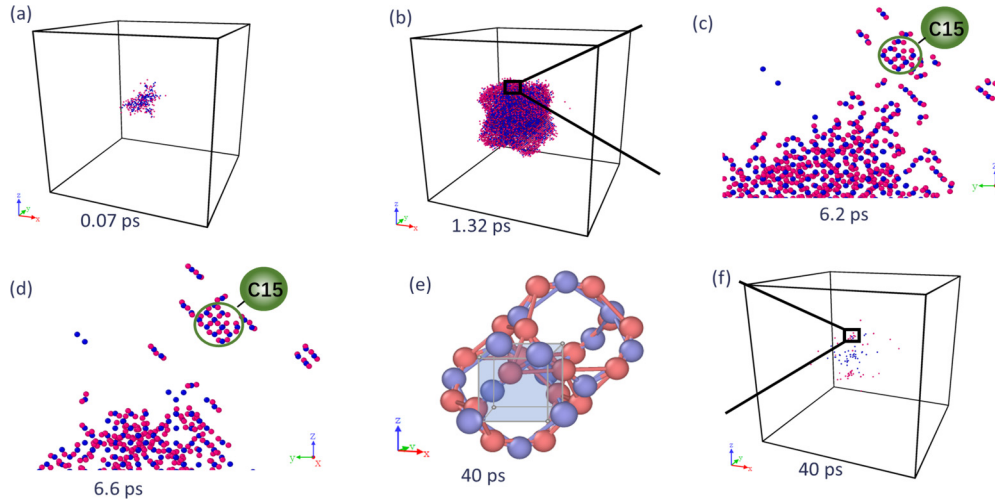
FIG. 1. Snapshots of the cascade process. A primary knocked-on atom with a kinetic energy of 50 keV at time zero moved along the ⟨235⟩ direction to initiate the cascade, with a sequence of (a) initial stage, (b) thermal spike, (c) C15 cluster nucleation, (d) formation, (e) enlarged I_4^{C15} interstitial clusters in stabilization, and (f) the final stage. In (a), (b), (e), and (f), only the defects are shown. The red particles represent the interstitial atoms and the blue particles are the vacancies. The snapshots of (c) and (d) were taken as side views along the ⟨001⟩ direction of the cubic system, with all position atoms partially exhibited for an enhanced view of the C15 cluster.

applied only along the X and Z directions, but a fixed boundary condition applied in the stress load Y direction, as suggested by previous studies [53–58]. Based on the convergence test for the yield stress, the strain rates were set to -0.001/ps and 0.001/ps to implement a uniaxial compression test and a tensile test, respectively.

B. Long-time evolution of the C15 cluster with accelerated molecular dynamics simulations

In this work, the self-adaptive accelerated molecular dynamics (SAAMD) method [41] was applied for long-time evolution of the C15 cluster formed in bcc tungsten. Chen's W-W potential [44] was also used for this purpose. The details determining the parameters used in SAAMD were provided in Refs. [41,42,59]. The boost potential could be obtained from the state of the atom on its harmonic vibration around its stable atomic position, as explained in Ref. [59], taking the following format:

$$
\begin{aligned}
V_{\text{bias}}&\big(\{r_1, \dots, r_{N_{\text{AV}}}\}; t\big) \\
&= E_b(t)\left\{1 - \left[\frac{\xi(\{r_1, \dots, r_{N_{\text{AV}}}\})}{q(t)}\right]^2\right\} \\
&\quad \times H\big[q(t) - \xi(\{r_1, \dots, r_{N_{\text{AV}}}\})\big],
\end{aligned} \tag{1}
$$

where E_b and q are parameters as a function of simulation time t. ξ is the total displacement of atoms in active volume (AV) within the system. Here, the AV was set within the one lattice constant from the outer part of the C15 cluster. Thus, the total number of atoms in AV was limited around 230–270 and the parameters, Δq and ΔE_b, were around 0.2 Å and 2.5–3.5 eV in SAAMD. The maximum displacement (D_{max}) in SAAMD was set around 4.5 Å based on pretesting calculations; this is large enough to ensure that the state will overcome the dividing surface to reach a lower-energy state. In SAAMD simulations, the simulation temperature was from

300 to 900 K. The displacement vector of each atom was calculated to demonstrate the phase transformation process for a C15 cluster. For each temperature simulation, 10 cases were simulations in which the random seed was changed to determine the initial temperature of the system in order to obtain the statistical results presented in the following section.

III. RESULTS AND DISCUSSION

A. The formation of C15 clusters in tungsten cascades

The displacement cascades in pure bcc W were performed via MD simulations at 363 K. An E_{PKA} of 20, 50, and 80 keV was considered within the simulation boxes containing 432 000–3 456 000 atoms, with the initial PKA directions starting at ⟨135⟩, ⟨235⟩, ⟨122⟩, ⟨133⟩, and ⟨111⟩ from the bottom left of the simulation box. Figure 1 shows the nucleation process of a C15 interstitial cluster during a displacement cascade process with $E_{\text{PKA}} = 50$ keV. In the majority of the images, only a part of the simulation cell is shown for clarity. Figure 1(a) illustrates the initial procedure, whereas Fig. 1(b) shows the thermal spike. The primary C15 cluster with two net interstitial atoms (I_2^{C15}) was rapidly generated in the cascade procedures, as shown in Fig. 1(c). Meanwhile, a small C15 cluster with four net interstitials (I_4^{C15}) was completely formed [Fig. 1(d)] through I_2^{C15} capturing the moving interstitials in the thermal spike at approximately 7 ps after the collision and stabilization. Figure 1(e) shows the detailed structure of I_4^{C15}, which exhibits a typical size of C15 clusters in W cascade processes, corresponding to 24 SIAs located at the edges of a truncated tetrahedron and surrounded by 20 vacancies, making a total of only four additional atoms in the bcc lattice, much like with C15 clusters in Fe [34]. Figures 1(c)–1(e) show the visible C15 cluster structures within the marked circles, whereas Fig. 1(f) shows a snapshot at a time of 40 ps. Here, when the simulation time was extended to 2 ns at 363 K, no significant change occurred in the C15 interstitial cluster. The above results indicated the direct formation of

an individual C15 interstitial cluster during the displacement cascades in bcc W. The nucleation of C15 clusters in W began immediately after the thermal spike at approximately 4 ps following the primary collision, whereas a complete individual I_4^{C15} cluster ultimately formed at approximately 7 ps. This is similar to previous work, where Chartier *et al.* [39] observed the C15 cluster appear in the very early stage of the microstructure evolution of irradiated Fe, prior to any loop. Once the individual C15 cluster has nucleated in W, it will remain highly stable and immobile at 30–1900 K, even when the simulation time is extended to 2 ns in classical MD.

Note that we observed the formation of C15 clusters in all the simulation PKA energies. Only two of the 20 cases involved an individual C15 cluster formed with an E_{PKA} of 20 keV, whereas this formation occurred in nine cases with an E_{PKA} of 50 keV and 14 with an E_{PKA} of 80 keV. It was found that the C15 clusters following the cascades were predominantly small in size (two to four SIAs). Moreover, the formation of C15 clusters was confirmed in almost all of the cascade simulations with a high-energy PKA of 100–300 keV and an energy step of 50 keV.

The dependence of C15 cluster formation on the interatomic potential was also tested using AT [60], JW [61], and MV4-S [62] potentials with $E_{\text{PKA}} = 50\,\text{keV}$ at room temperature (300 K). Here, C15 clusters were observed in the displacement cascade processes produced by all the potentials, and they were predominately small in size. The cascade simulations with high PKA energy returned similar results. Furthermore, the formation energies of the ⟨111⟩, ⟨100⟩, and C15 clusters were calculated according to the potentials, as shown in Fig. 2, and then compared with the DFT results [40]. Clearly, the smaller-size C15 clusters were energetically more favorable in W, as predicted by all the potentials. In terms of the DFT at small sizes (<20 SIA), the formation energy of the C15 cluster was higher than that of the ⟨111⟩ clusters and lower than that of the ⟨100⟩ clusters. The C15 cluster predicted by the AT and JW potentials exhibited higher formation energy than did the ⟨111⟩ and ⟨100⟩ clusters at all sizes, with the formation energy difference between the C15 and the loops increasing sharply with the increase in the size of the cluster. Moreover, for the Chen and MV4-S potentials, small-sized C15 clusters (<20 SIA) were found to be energetically more favorable than the ⟨111⟩ clusters, whereas the relative stabilities were reversed beyond a comparatively large size of approximately 20–40 SIAs. Although the formation energy calculated via DFT suggested that the C15 cluster in the W was not the lowest in terms of energy, the formation of C15 structures in the cascade processes was observed in terms of all the potentials, which can be attributed to the nonequilibrium irradiation-induced processes, where high temperatures and high pressures could appear locally at the cascading center [5], providing suitable conditions for the formation of C15 clusters. The probability of C15 formation was estimated to be approximately 5–45 % across the 20 cascade simulations, as obtained by different interatomic potentials with $E_{\text{PKA}} = 50\,\text{keV}$ at 300 K, with the minimum and maximum values corresponding to the results of the AT and the Chen/MV4-S potentials, respectively. Therefore, the nucleation of C15 clusters should be a general phenomenon in cascades involving W.

B. Transformation of C15 clusters into ⟨111⟩ loops at high temperature with classical molecular dynamics and accelerated molecular dynamics

To gain further insight into the C15 clusters formed in W, we investigated not only the evolution of the C15 cluster following the cascades, but also the stability of different-sized C15 clusters. When the high-temperature classical MD relaxation was performed for the predominant C15 cluster (I_4^{C15}) of Fig. 1 formed in the cascade processes, the cluster was found to directly transform into a ⟨111⟩ cluster until the temperature reached approximately 3000 K after a few hundred picoseconds. To confirm this transformation, various different-sized C15 clusters (I_2^{C15}, I_4^{C15}, I_{11}^{C15}, I_{30}^{C15}, and I_{40}^{C15}) were selected as the models for investigating the properties of the C15 clusters at high temperatures. Much like with the transformation of the typical C15 cluster obtained via the cascades, when the different-sized C15 clusters underwent the high-temperature relaxation processes from 1000 to 3400 K and when the simulation time was extended to 2 ns at each temperature, the I_2^{C15}, I_4^{C15}, I_{30}^{C15}, and I_{40}^{C15} clusters began to transform into ⟨111⟩ clusters/loops at critical temperature points of approximately 2000, 3000, 3200, and 2800 K in the classical MD. This indicates that a high temperature is an important factor for the transformation of C15 clusters into ⟨111⟩ loops/clusters.

However, for the I_{11}^{C15} cluster, we observed no direct transformation behavior, which may have been because of the timescale limitation of classical MD simulations. Therefore, in the present work, AMD simulations were conducted to provide a longer timescale simulation for investigating the evolution of C15 clusters. As such, the transformation of I_{11}^{C15} clusters into ⟨111⟩ loops/clusters could be observed. Moreover, the stability of the C15 clusters was also examined using the JW potential in high-temperature classical MD. Here, it was found that with a JW potential, the C15 clusters could transform into ⟨100⟩ loops at low temperatures before ultimately transforming into ⟨111⟩ loops at comparatively high temperatures (>1000 K), which may have been because of the small formation energy difference between the ⟨111⟩ and ⟨100⟩ dislocation loops of the JW potential, as shown in Fig. 2. This is similar to the phenomenon in Fe observed by Chartier *et al.* [39]. They reported that both $1/2\langle 111\rangle$ and ⟨100⟩ loops can directly nucleate from C15 clusters in Fe, and in the present work, only the $1/2\langle 111\rangle$ loops can directly nucleate from C15 clusters in W. This may be due to the small formation energy difference between $1/2\langle 111\rangle$ and ⟨100⟩ loops of the M07 potentials in Fe [63], where there is a relatively large formation energy difference of the Chen potentials in W, indicating that $1/2\langle 111\rangle$ loops are energetically more favorable in W, as shown in Fig. 2.

We further validated this transformation from C15 clusters to ⟨111⟩ clusters/loops in W using the AMD method with a comparatively longer timescale evolution. Here, the I_{11}^{C15} cluster is taken as an example. Three possible decomposition mechanisms of C15 clusters were proposed. As shown in Fig. 3 in relation to Mechanism (I), the I_{11}^{C15} cluster could directly transform into a $1/2\langle 111\rangle$ interstitial dislocation loop, which was consistent with the high-temperature classical MD simulations. Figure 4 shows the details of the structure and the atom displacement of Mechanism (I). See the Supplemental
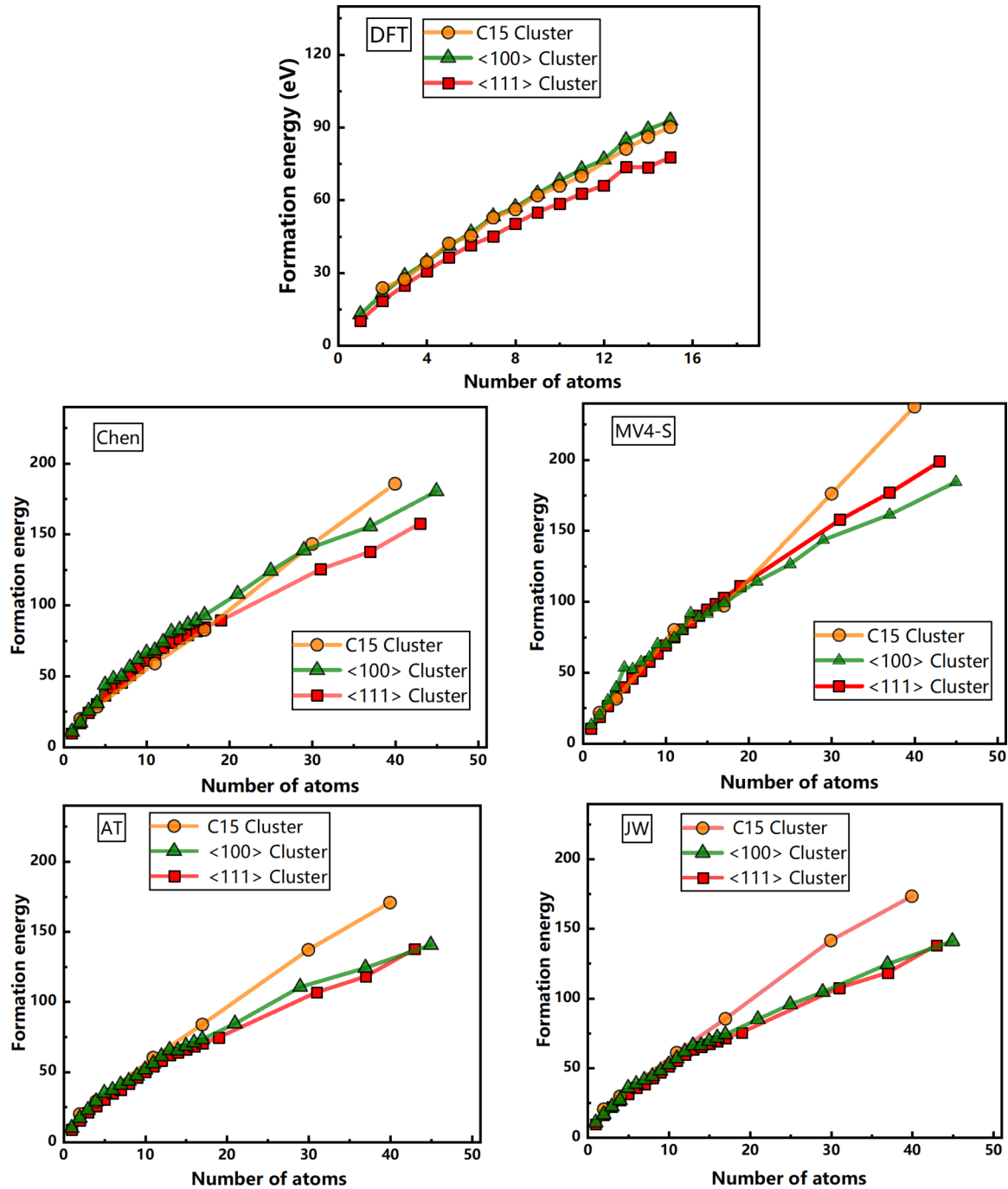
FIG. 2. The formation energy of ⟨111⟩, ⟨100⟩, and C15 clusters calculated via DFT [40] and the interatomic potentials.

Material [64] (Movie-1) for the whole process of Mechanism (I). First, the boundary atoms in the C15 clusters transformed into ⟨111⟩ dumbbells, whereas the center atoms in the I_{11}^{C15} cluster exhibited a trend of migrating along the ⟨110⟩ direction before the collapse. The transformed ⟨111⟩ dumbbells would drive other atoms to move along the ⟨111⟩ direction before a complete 1/2⟨111⟩ interstitial loop was ultimately formed. As shown in Fig. 3 in relation to Mechanism (II), the C15 clusters could be transformed into a small mobile ⟨111⟩ cluster/loop, leaving a smaller C15 cluster. See the Supplemental Material [64] (Movie-2) for the whole process of Mechanism (II). This means that a portion of the atoms in C15 clusters can

transform into ⟨111⟩ clusters, becoming free individual SIA clusters/loops far removed from the C15 clusters. Meanwhile, the remaining atoms could still retain C15 structures, whereas the shrunken and immobile C15 cluster could be transformed into ⟨111⟩ clusters/loops with further evolution, and this is one possible state of the pinned loops and small-sized clusters observed in previous experiments [13,14]. As shown in Fig. 3 in relation to Mechanism (III), clearly there existed a stable configuration of a pinned ⟨111⟩ cluster/loop near a shrunken C15 cluster. See the Supplemental Material [64] (Movie-3) for the whole process of Mechanism (III). Much like with Mechanism (II), several atoms in the C15 clusters transformed
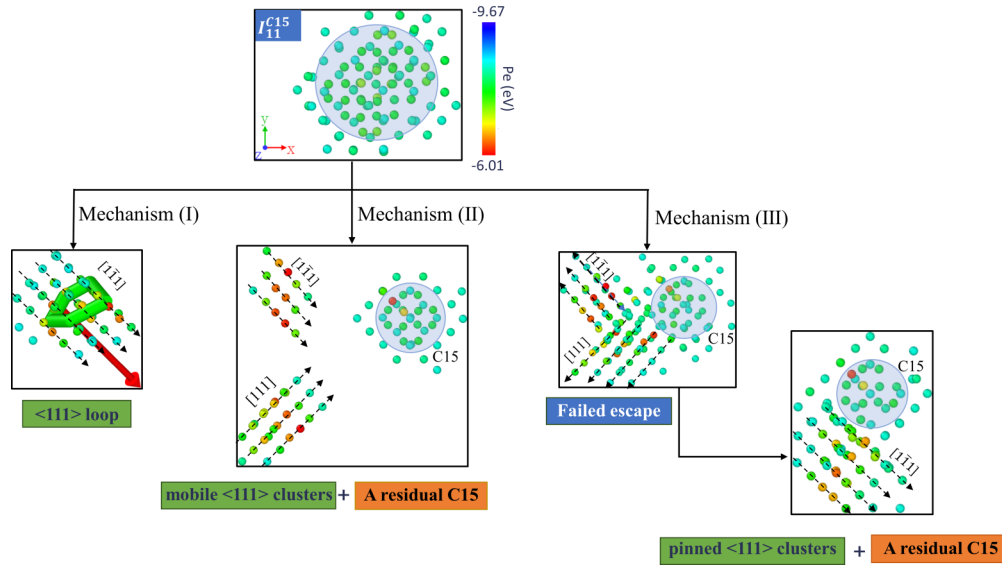
FIG. 3. Three possible transform mechanisms of C15 clusters. The structure types were analyzed via the common neighbor analysis method, with only the non-bcc atoms shown. Here, the atoms are colored in terms of their potential energies, with the corresponding colors shown in the color bar. The green line and the red arrow represent the $1/2\langle 111 \rangle$ dislocation loop and the Burgers vector, respectively.

into $\langle 111 \rangle$ clusters/loops successfully but then failed to escape away from the C15 cluster, largely pinned by the C15 cluster to form a complicated loop-C15 structure. This phenomenon was similar to that observed in the following MD simulations of the interaction between the $\langle 111 \rangle$ dislocation loops and the C15 clusters, where the $\langle 111 \rangle$ interstitial loop was found to be pinned by the C15 clusters and is one possible state of the pinned loops and small-sized clusters observed in previous experiments. Moreover, the timescale of SAAMD depends on the simulation temperatures. In this work, for example, at around 700 K, the transformation is observed with time up

to around the second timescale. After obtaining enough statistical results, the related frequency as a function of $1/T$ can be obtained. Thus, with the Arrhenius equation, the energy barrier can be obtained. One example is shown in Fig. 5. The energy barrier is around 1.97 eV obtained with the fitted slope of the curve.

According to previous studies [12,36,65], for a loop with an effective radius R, the formation energy E_f (per SIA) can be obtained as follows:

$$E_f = 2\Omega \left(F_t \ln\frac{4R}{e\delta} + F_\delta + F_c \right) \Big/ Rb, \qquad (2)$$
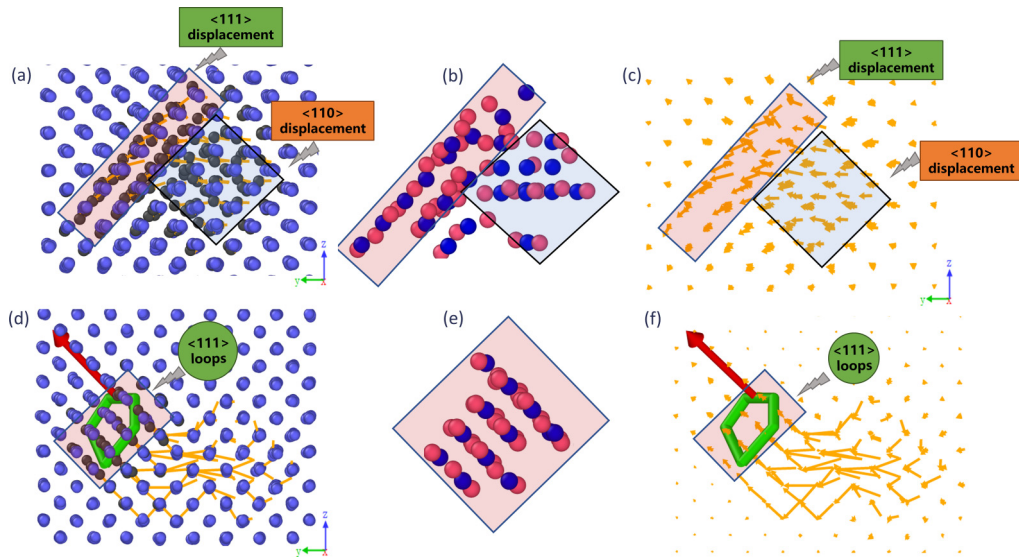

FIG. 4. Structure of (a) I_{11}^{C15} clusters starting to transform and (d) after collapsing into a $\langle 111 \rangle$ dislocation loop. Here, (b) and (e) show the defects of the interstitial atoms (red ball) and vacancies (blue ball), whereas (c) and (f) enlarge the displacement of (a) and (b), respectively. The atoms in (a) and (d) are colored in relation to the DXA analysis, with the bcc atoms shown in blue and the others in black. The orange lines represent the displacement of the atoms, whereas the green line and the red arrow represent the $1/2\langle 111 \rangle$ dislocation loop and the Burgers vector, respectively.
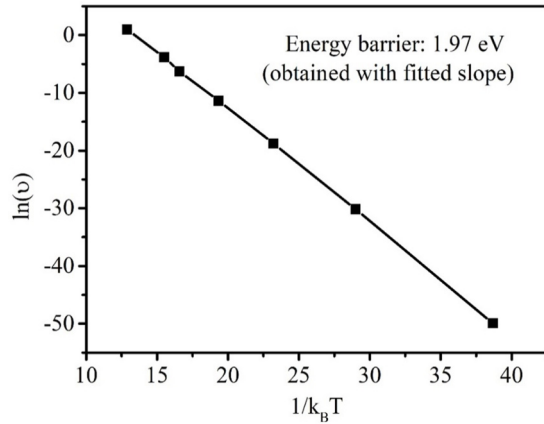
FIG. 5. The energy barrier for the transformation of the C15 clusters into ⟨111⟩ loops.

where Ω is the atomic volume of the bcc atom; e is a constant; δ and b are the core width and the Burgers vector, respectively; and F_t, F_δ, and F_c are the prelogarithmic factors for a dislocation, the anharmonic core, and the core-traction energy, respectively.

For a C15 cluster, assuming a spherical, coherent inclusion in an isotropic matrix [66], the E_f can be calculated as follows [36]:

$$E_f = \frac{6\Omega\,\gamma}{R} + \frac{12\mu\,\Omega\varepsilon^2}{\alpha} + 3\left(E_{\text{coh}}^{\text{bcc}} - E_{\text{coh}}^{\text{C15}}\right), \qquad (3)$$

where γ is the effective interfacial energy, μ is the shear modulus of the matrix, ε is the misfit strain, α is a constant given by the elastic moduli of bulk bcc and C15 phases, and $E_{\text{coh}}^{\text{bcc}}$ and $E_{\text{coh}}^{\text{C15}}$ are the corresponding cohesive energies. The three terms in Eq. (3), respectively, indicate the interfacial energy, elastic strain energy, and cohesive energy of the C15 phase relative to the bcc phase. Clearly, the formation energies of the loops [Eq. (2)] and C15 clusters [Eq. (3)] were size dependencies. In terms of the loops, the E_f decreased approximately in line with $\ln\frac{4R}{e\delta}/R$, approaching zero at $R \to \infty$. Meanwhile, in terms of the C15 clusters, the first term decreased in line with $1/R$ and tended to be negligible at larger sizes, whereas the strain ε and cohesive energies were size-independent, with their total giving E_f at $R \to \infty$. Therefore, the loops were more stable than the C15 clusters at larger sizes, where the transformation from C15 clusters into loops may be feasible.

The smaller C15 clusters were found to be energetically more favorable in W, as shown in Fig. 2, which was consistent with the predominantly small-sized C15 clusters following the cascades. These small C15 clusters can grow by absorbing mobile SIAs and transform into loops at sizes and times below those characterized via TEM, thus explaining their absence in the experiments, which is expected to be explored by the higher-level characterization in future, such as pulsed laser-combined scanning tunneling microscopy [67]. In the present work, both classical MD and AMD allowed for observing this transformation, and a possible mechanism for ⟨111⟩ interstitial loop formation could thus be proposed, which can give valuable insight into the physical mechanisms of the dislocation loop formation.
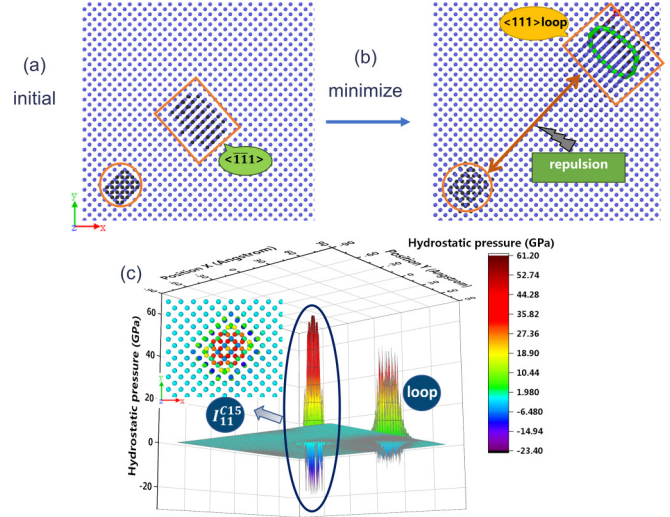

FIG. 6. The configuration of the ⟨111⟩ cluster far from the C15 cluster at (a) initial distance of 8 Å and (b) the ground-state configuration after minimization. The bcc atoms are shown in blue and the others in black, whereas the green lines and the red arrow represent the $1/2\langle111\rangle$ dislocation loop and the Burgers vector, respectively. (c) The hydrostatic pressure of atoms in the systems. Here, the atoms are colored in terms of hydrostatic pressure, with the corresponding colors shown in the color bar.

C. The interaction between C15 clusters and dislocation loops/vacancy clusters

Following cascade procedures, various typical defect clusters, such as dislocation loops and vacancy clusters, typically appear in the materials [1,5–7,48] and effect the evolution of the microstructure of materials [68]. To better understand the effect of these defect clusters on C15 clusters during their evolution, we investigated the interaction between typical radiation-damaged defect clusters (including ⟨111⟩ interstitial loops and vacancy clusters) and C15 clusters. First, when the ⟨111⟩ loop and the C15 cluster are located on the same plane as the Burgers vector of the ⟨111⟩ loop pointing to the C15 cluster, the approaching behavior of the nonadjacent $1/2\langle111\rangle$ dislocation loops and the C15 cluster cannot be observed in MD at 1000 K, even when the simulation time is extended to 4 ns. Thus, the distribution of the attendant hydrostatic pressure was calculated, with the results shown in Fig. 6. Here, it was clear that a positive hydrostatic pressure was located inside the loop and the I_{11}^{C15} clusters, and that a negative hydrostatic pressure surrounded both, which is a similar situation to the stress distribution of interstitial loops in Fe [69]. Thus, a strong repulsive interaction exists between them, which may be why it is almost impossible for loops and C15 clusters to approach each other before overcoming the strong repulsive barrier. However, when the loop was tangent to the C15, that is, the Burgers vector was not along the line connecting the two defects, the loop could be absorbed by the C15 cluster once it had moved within a certain range, forming a complicated loop-C15 structure. A similar configuration can be obtained after a cascade procedure, with a ⟨111⟩ interstitial dislocation loop located near the I_4^{C15} clusters, as shown in Fig. 7(a). Here, the adjacent loop will be pinned
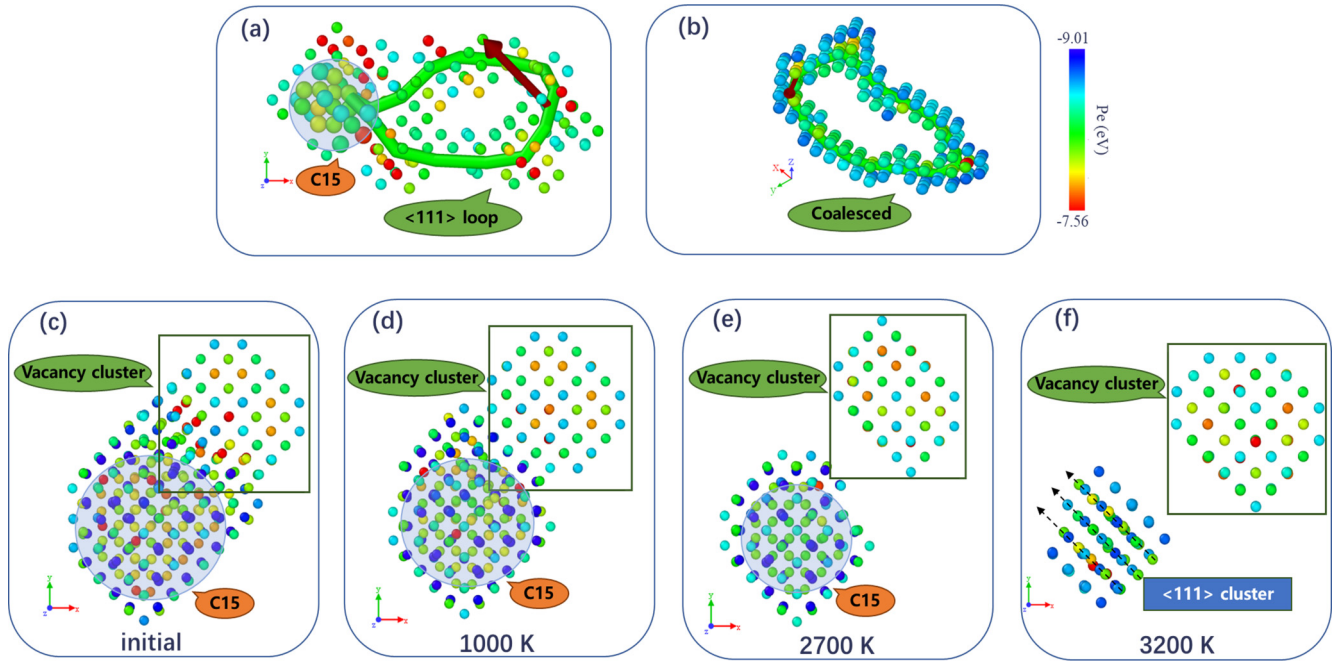
FIG. 7. (a) The configuration of the $\langle 111 \rangle$ loop located near the I_4^{C15} cluster after cascades of 363 K, the C15 atoms are colored with a larger size. (b) The configuration of a larger $\langle 111 \rangle$ loop coalesced by the $\langle 111 \rangle$ loop and the C15 cluster at 2000 K. The green lines and the red arrow represent the $1/2\langle 111 \rangle$ dislocation loops and the Burger vectors of $1/2\langle 111 \rangle$, respectively. The configuration of the vacancy cluster with 60 vacancies located near the I_{40}^{C15} cluster of (c) the initial structure and extended to 1 ns at various temperatures of (d) 1000 K, (e) 2700 K, and (f) 3200 K. For clarity, the configuration presented here is that obtained after quenching. The structure types were analyzed via the common neighbor analysis method, with only the non-bcc atoms shown. The atoms are colored in terms of their potential energies, with the corresponding colors shown in the color bar.

by the C15 cluster at low temperatures, with its migration suppressed even when the simulation time is extended to 2 ns, forming a complicated loop-C15 structure, which is consistent with the phenomenon observed during the AMD simulations related to Mechanism (III) (Fig. 3). Moreover, they tended to coalesce to a larger loop at a high temperature within a few hundred picoseconds in the MD, as shown in Fig. 7(b). Note that the interaction between the dislocation loops and the C15 will facilitate the transformation of C15 clusters into $\langle 111 \rangle$ dislocation loops/clusters at a lower temperature (2000 K for I_4^{C15}) than without the dislocation loop (3000 K). These results mean that C15 clusters may affect the defect cluster mobility and kinetics of the microstructure, which can provide important knowledge regarding the microstructural evolution in W.

During the cascade processes, numerous dislocation loops tended to form close to the C15 clusters. We also examined various combinations of different-sized loops located close to different-sized C15 clusters, similar to the configuration shown in Fig. 7(a). When a comparatively large-sized loop (with 45 interstitials) appeared close to a small I_4^{C15} or a large I_{40}^{C15} cluster, the coalescence of a larger loop was observed for both cases. Meanwhile, the larger the size of the C15 clusters, the easier they could coalesce, which transformed into a larger $\langle 111 \rangle$ interstitial loop at 2000 and 1500 K for this large-sized loop close to the I_4^{C15} and I_{40}^{C15} clusters, respectively. Unlike the large-sized loop and C15 cluster reaction, where the C15 cluster and loop are generally easily coalesced, the combination of small-sized loops (with seven interstitials) and C15 clusters (I_4^{C15} or I_{11}^{C15}) will result in the absorption of

the loops and the growth of the C15 clusters, unless the size of the C15 cluster was so large that the absorption behavior approached saturation. For example, we found that the comparatively large-sized I_{40}^{C15} cluster barely absorbed the loops, which tended to coalesce and transform into a larger loop.

Meanwhile, we also considered the interaction between the C15 clusters and an adjacent vacancy cluster. The configuration of an I_{40}^{C15} cluster adjoining a vacancy cluster with 60 vacancies is shown in Fig. 7(c)–7(f) with the initial structure shown in Fig. 7(c), whereas Figs. 7(d)–7(f) show the configuration after a 1 ns evolution at 1000, 2700, and 3200 K, respectively. As shown in Figs. 7(d) and 7(e), the adjacent vacancy cluster will likely influence the stability of the C15 structures. The size of the C15 cluster shrank with the increase in temperature, indicating that a portion of the I_{40}^{C15} clusters had been absorbed by the adjacent vacancy clusters. The residual shrunken C15 clusters (not adjacent to the vacancy clusters) tended to transform into $\langle 111 \rangle$ clusters, as shown in Fig. 7(f), much like with the direct transformation mechanism in the high-temperature classical MD and AMD related to Mechanism (I). If the small C15 cluster (I_2^{C15} or I_4^{C15}) adjoins a vacancy cluster, it will likely be completely absorbed by vacancy clusters at approximately 1000 K.

In addition, the higher-level multiscale simulations, such as kinetic Monte Carlo, cluster dynamics, or discrete dislocation dynamics, are necessary and will be important in the future to better explore the role of C15 in producing microstructures due to high doses of irradiation, which can simulate not only a single dislocation and few defects but also collective dislocation processes. In addition, they can be used to obtain
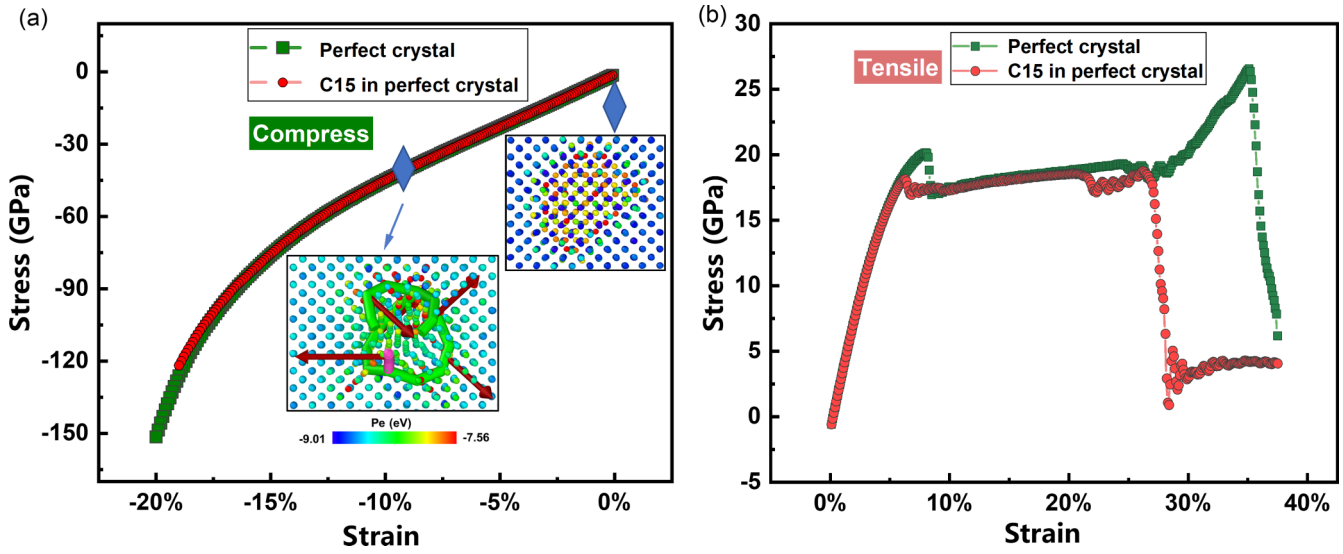
FIG. 8. Stress-strain curves corresponding to the perfect crystal and the system containing C15 clusters: (a) compression processes and (b) tensile processes. The atoms in (a) are colored in terms of potential energy, with the corresponding colors shown in the color bar. The pink lines, the green lines, and the red arrow represent ⟨100⟩ dislocation loops, $1/2\langle111\rangle$ dislocation loops, and the Burgers vector, respectively.

important knowledge of the mechanical properties of irradiated materials [70].

D. The effects of compression/tensile stresses on C15 clusters

In fact, the stress field may exist under the radiation damage condition, which would affect the behavior of defects and the properties of the materials [53–58,71–73]. To confirm the transformation mechanism obtained via the classical MD and AMD simulations, the stability of a C15 cluster was simulated under the stress field at room temperature. Here, the large-sized C15 cluster (I_{40}^{C15}) was considered to explore the behavior of a C15 cluster and its effect on the material. All deformation simulations were performed using MD, and the strain rates were set to $-0.001/\mathrm{ps}$ and $0.001/\mathrm{ps}$ along the Y direction for implementing a uniaxial compression test and a uniaxial tensile test, respectively. The stress-strain curves of a W crystal containing a large C15 cluster (I_{40}^{C15}) and a perfect W crystal were obtained. The corresponding resolved normal stress and strain induced by the applied deformation were given by [54,72]

$$\sigma_{yy} = \frac{F_{yy}}{A_{xz}}, \qquad (4)$$

$$\varepsilon = \frac{L - L_0}{L_0}, \qquad (5)$$

where F_{yy} is the total force acting in the Y direction of atoms, A_{xz} is the XZ cross-section area of the box, L is the instantaneous length along the Y-direction, and L_0 is the initial length in the Y-direction.

As shown in Fig. 8(a), during the compression processes, although little difference was observed between the stress-strain curve of the system containing the C15 clusters and the perfect crystal, the initial C15 clusters clearly transformed into a $1/2\langle111\rangle$ interstitial dislocation loop, with the loop that can grow along the direction of the Burgers vector with the increase in strain. Figure 9 presents the details of the structural

evolution of the C15 clusters during the compression stress test. An initial transformation from partial C15 cluster to ⟨111⟩ loop occurred at $\varepsilon = -0.084$, with the remaining portion also transforming at $\varepsilon = -0.16$, which was similar to the transformation behavior of Mechanism (II) (Fig. 3) obtained via AMD. During the tensile processes, the atomic structure of the C15 cluster exhibited no significant change until the materials fractured, with Fig. 8(b) showing the comparison of the stress-strain curve for the system containing C15 structures and the perfect crystal. The system containing C15 clusters
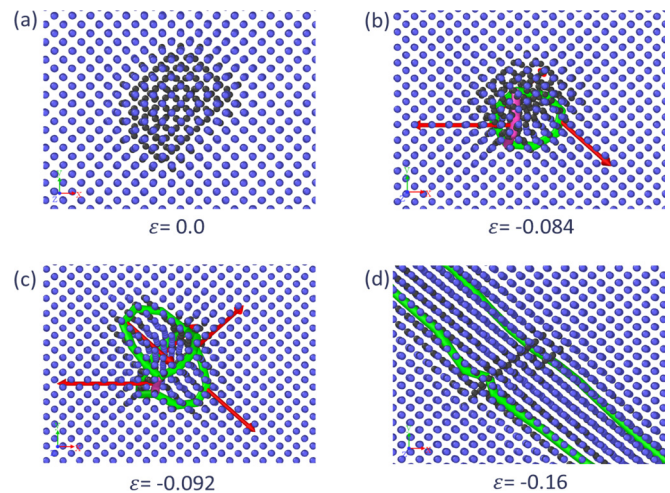

FIG. 9. Snapshots of the structure of C15 clusters under the process of compression testing at 300 K: (a) $\varepsilon = 0.0$, the initial C15 structure; (b) $\varepsilon = -0.084$, the C15 cluster collapsing into dislocation loops; (c) $\varepsilon = -0.092$, the growth of a portion of the dislocation loops; (d) $\varepsilon = -0.16$, the growth of another portion of the dislocation loops. The bcc atoms are shown in blue and the others in black. The pink lines, the green lines, and the red arrow represent ⟨100⟩ dislocation loops, $1/2\langle111\rangle$ dislocation loops, and the Burgers vector, respectively.

fractured close to the C15 cluster region at $\varepsilon = 0.26$, with a tensile strength of 18.8 GPa, whereas the perfect crystal system fractured at $\varepsilon = 0.35$, with a tensile strength of 26.6 GPa. From this view, it seems that the large C15 clusters may impede the plastic deformation and result in the brittleness of the materials. However, under irradiation, the C15 clusters can quickly transform to loop structures, especially for large-sized C15 clusters. Thus, the C15 clusters actually have a limited impact on material deformation.

IV. CONCLUSION

In this paper, the formation mechanism of $\langle 111 \rangle$ interstitial loops, and the nucleation and stability of C15 in W, were investigated. The nucleation of C15 clusters occurs in only a few picoseconds, and it remains highly stable and immobile within a displacement cascade, which is a general phenomenon that is independent of the interatomic potential. The transformation from C15 clusters to $\langle 111 \rangle$ interstitial loops was observed during high-temperature classical MD and AMD simulations. Three possible transformation processes were observed: C15 clusters (i) directly collapse into the $\langle 111 \rangle$ interstitial dislocation loops, (ii) partially collapse into the $\langle 111 \rangle$ interstitial dislocation loops with high mobility, thus leaving shrunken C15 clusters behind, and (iii) partially collapse into the $\langle 111 \rangle$ interstitial dislocation loops but pinned by an adjacent shrunken C15 cluster. In addition, this transformation was further confirmed when a compressive stress field was applied, and it can be accelerated once the $\langle 111 \rangle$ interstitial loops react with the C15 clusters. Based on these results, we reported a possible formation mechanism of $1/2\langle 111 \rangle$ interstitial dislocation loops via the collapse of C15 clusters in W. This formation mechanism provides important knowledge regarding $\langle 111 \rangle$ interstitial loop formation, as well as insights into the engineering microstructural evolution in W.

[1] K. Nordlund and R. S. Averback, Phys. Rev. B **56**, 2421 (1997).

[2] R. E. Stoller, G. R. Odette, and B. D. Wirth, J. Nucl. Mater. **251**, 49 (1997).

[3] D. J. Bacon, F. Gao, and Y. N. Osetsky, J. Nucl. Mater. **276**, 1 (2000).

[4] Y. Matsukawa and S. J. Zinkle, Science **318**, 959 (2007).

[5] Q. Peng, F. Meng, Y. Yang, C. Lu, H. Deng, L. Wang, S. De, and F. Gao, Nat. Commun. **9**, 4880 (2018).

[6] Y. Lin, T. Yang, L. Lang, C. Shan, H. Deng, W. Hu, and F. Gao, Acta Mater. **196**, 133 (2020).

[7] C. Shan, L. Lang, T. Yang, Y. Lin, F. Gao, H. Deng, and W. Hu, Comput. Mater. Sci. **177**, 109555 (2020).

[8] J. Silcox and P. B. Hirsch, Philos. Mag. **4**, 1356 (1959).

[9] K. Nordlund and F. Gao, Appl. Phys. Lett. **74**, 2720 (1999).

[10] K. Arakawa, K. Ono, M. Isshiki, K. Mimura, M. Uchikoshi, and H. Mori, Science **318**, 956 (2007).

[11] B. C. Masters, Nature (London) **200**, 254 (1963).

[12] S. L. Dudarev, R. Bullough, and P. M. Derlet, Phys. Rev. Lett. **100**, 135503 (2008).

[13] X. Yi, M. L. Jenkins, M. Briceno, S. G. Roberts, Z. Zhou, and M. A. Kirk, Philos. Mag. **93**, 1715 (2013).

[14] X. Yi, M. L. Jenkins, K. Hattar, P. D. Edmondson, and S. G. Roberts, Acta Mater. **92**, 163 (2015).

[15] X. Yi, M. L. Jenkins, M. A. Kirk, Z. Zhou, and S. G. Roberts, Acta Mater. **112**, 105 (2016).

[16] T. D. de la Rubia, N. Soneda, M. J. Caturla, and E. A. Alonso, J. Nucl. Mater. **251**, 13 (1997).

[17] Y. N. Osetsky, D. J. Bacon, A. Serra, B. N. Singh, and S. I. Golubov, J. Nucl. Mater. **276**, 65 (2000).

[18] F. Gao, D. J. Bacon, L. M. Howe, and C. B. So, J. Nucl. Mater. **294**, 288 (2001).

[19] Y. N. Osetsky, D. J. Bacon, A. Serra, B. N. Singh, and S. I. Golubov, Philos. Mag. A **83**, 61 (2003).

[20] J. Byggmastar, F. Granberg, A. E. Sand, A. Pirttikoski, R. Alexander, M. C. Marinica, and K. Nordlund, J. Phys.: Condens. Matter **31**, 245402 (2019).

[21] Y. N. Osetsky, D. J. Bacon, and A. Serra, Philos. Mag. Lett. **79**, 273 (1999).

[22] K. Arakawa, T. Amino, and H. Mori, Acta Mater. **59**, 141 (2011).

[23] J. Chen, N. Gao, P. Jung, and T. Sauvage, J. Nucl. Mater. **441**, 216 (2013).

[24] H. Kurishita, S. Matsuo, H. Arakawa, T. Sakamoto, S. Kobayashi, K. Nakai, G. Pintsuk, J. Linke, S. Tsurekawa, V. Yardley, K. Tokunaga, T. Takida, M. Katoh, A. Ikegaya, Y. Ueda, M. Kawai, and N. Yoshida, Mater. Trans. **54**, 456 (2013).

[25] A. E. Sand, S. L. Dudarev, and K. Nordlund, Europhys. Lett. **103**, 46003 (2013).

[26] L. K. Béland, Y. N. Osetsky, R. E. Stoller, and H. Xu, J. Alloys Compd. **640**, 219 (2015).

[27] X. Hu, T. Koyanagi, M. Fukuda, N. A. P. K. Kumar, L. L. Snead, B. D. Wirth, and Y. Katoh, J. Nucl. Mater. **480**, 235 (2016).

[28] C. Fu, J. D. Torre, F. Willaime, J. L. Bocquet, and A. Barbu, Nat. Mater. **4**, 68 (2005).

[29] Y. Chen, J. Fang, L. Liu, W. Hu, C. Jiang, N. Gao, H. Zhou, G. Lu, F. Gao, and H. Deng, J. Nucl. Mater. **522**, 200 (2019).

[30] D. Rodney and G. Martin, Phys. Rev. Lett. **82**, 3272 (1999).

[31] T. D. de la Rubia, H. M. Zbib, T. A. Khraishi, B. D. Wirth, M. Victoria, and M. J. Caturla, Nature (London) **406**, 871 (2000).

[32] G. S. Was, Mater. Today **10**, 52 (2007).

[33] F. Gao, D. J. Bacon, Y. N. Osetsky, P. E. J. Flewitt, and T. A. Lewis, J. Nucl. Mater. **276**, 213 (2000).

[34] M. C. Marinica, F. Willaime, and J. P. Crocombette, Phys. Rev. Lett. **108**, 025501 (2012).

[35] L. Dézerald, M. C. Marinica, L. Ventelon, D. Rodney, and F. Willaime, J. Nucl. Mater. **449**, 219 (2014).

[36] Y. Zhang, X. Bai, M. R. Tonks, and S. B. Biner, Scr. Mater. **98**, 5 (2015).

[37] R. Alexander, L. Proville, C. S. Becquart, A. M. Goryeava, J. Dérès, C. Lapointe, and M. C. Marinica, J. Nucl. Mater. **535**, 152141 (2020).

[38] J. Byggmästar and F. Granberg, J. Nucl. Mater. **528**, 151893 (2020).

[39] A. Chartier and M. C. Marinica, Acta Mater. **180**, 141 (2019).

[40] J. Byggmästar, A. Hamedani, K. Nordlund, and F. Djurabekova, Phys. Rev. B **100**, 144105 (2019).

[41] N. Gao, L. Yang, F. Gao, R. J. Kurtz, D. West, and S. Zhang, J. Phys.: Condens. Matter **29**, 145201 (2017).

[42] N. Gao, Z. Yao, G. Lu, H. Deng, and F. Gao, Nat. Commun. **12**, 225 (2021).

[43] S. Plimpton, J. Comput. Phys. **117**, 1 (1995).

[44] Y. Chen, Y. Li, N. Gao, H. Zhou, W. Hu, G. Lu, F. Gao, and H. Deng, J. Nucl. Mater. **502**, 141 (2018).

[45] L. Liu, Y. Chen, R. Qiu, W. Hu, and H. Deng, At. Energy Sci. Technol. **51**, 8 (2021).

[46] L. Liu, X. Li, Y. Chen, W. Hu, G. Luo, F. Gao, and H. Deng, Tungsten **2**, 3 (2020).

[47] J. F. Ziegler and J. P. Biersack, in *Treatise on Heavy-Ion Science*, edited by D. A. Bromley (Springer, Boston, 1985), p. 93.

[48] J. Fu, Y. Chen, J. Fang, N. Gao, W. Hu, C. Jiang, H. Zhou, G. Lu, F. Gao, and H. Deng, J. Nucl. Mater. **524**, 9 (2019).

[49] R. E. Stoller, J. Nucl. Mater. **276**, 22 (2000).

[50] G. J. Martyna, M. L. Klein, and M. Tuckerman, J. Chem. Phys. **97**, 2635 (1992).

[51] A. Stukowski, Modell. Simul. Mater. Sci. Eng. **18**, 015012 (2009).

[52] A. Stukowski, V. V. Bulatov, and A. Arsenlis, Modell. Simul. Mater. Sci. Eng. **20**, 085007 (2012).

[53] L. Liu, Y. Chen, N. Gao, W. Hu, S. Xiao, F. Gao, and H. Deng, Comput. Mater. Sci. **173**, 109412 (2020).

[54] J. Shi, L. Peng, M. Ye, and F. Gao, IEEE Trans. Plasma Sci. **45**, 289 (2017).

[55] J. He, G. Tang, A. Hasegawa, and K. Abe, Nucl. Fusion **46**, 877 (2006).

[56] X. Bai, A. F. Voter, R. G. Hoagland, M. Nastasi, and B. P. Uberuaga, Science **327**, 1631 (2010).

[57] M. A. Tschopp, M. F. Horstemeyer, F. Gao, X. Sun, and M. Khaleel, Scr. Mater. **64**, 908 (2011).

[58] M. A. Tschopp, K. N. Solanki, F. Gao, X. Sun, M. A. Khaleel, and M. F. Horstemeyer, Phys. Rev. B **85**, 064108 (2012).

[59] J. Chen, P. Jung, W. Hoffelner, and H. Ullmaier, Acta Mater. **56**, 250 (2008).

[60] G. J. Ackland and R. Thetford, Philos. Mag. A **56**, 15 (1987).

[61] N. Juslin and B. D. Wirth, J. Nucl. Mater. **432**, 61 (2013).

[62] W. Setyawan, N. Gao, and R. J. Kurtz, J. Appl. Phys. **123**, 205102 (2018).

[63] L. Malerba, M. C. Marinica, N. Anento, C. Björkas, H. Nguyen, C. Domain, F. Djurabekova, P. Olsson, K. Nordlund, A. Serra, D. Terentyev, F. Willaime, and C. S. Becquart, J. Nucl. Mater. **406**, 19 (2010).

[64] See Supplemental Material at http://link.aps.org/supplemental/10.1103/PhysRevMaterials.5.093605 for three movies detailing the three possible transformation mechanisms of C15 clusters.

[65] D. J. Bacon, R. Bullough, and J. R. Willis, Philos. Mag. **22**, 31 (1970).

[66] J. D. Eshelby, in *Solid State Physics*, edited by F. Seitz and D. Turnbull (Academic, New York, 1956), p. 79.

[67] C. Guo, X. Meng, H. Fu, Q. Wang, H. Wang, Y. Tian, J. Peng, R. Ma, Y. Weng, S. Meng, E. Wang, and Y. Jiang, Phys. Rev. Lett. **124**, 206801 (2020).

[68] P. M. Derlet and S. L. Dudarev, Phys. Rev. Mater. **4**, 023605 (2020).

[69] Y. Li, S. Hu, C. H. Henager, H. Deng, F. Gao, X. Sun, and M. A. Khaleel, J. Nucl. Mater. **427**, 259 (2012).

[70] A. Lehtinen, L. Laurson, F. Granberg, K. Nordlund, and M. J. Alava, Sci. Rep. **8**, 6914 (2018).

[71] D. M. Clatterbuck, D. C. Chrzan, and J. W. Morris, Acta Mater. **51**, 2271 (2003).

[72] D. Terentyev and X. He, Comput. Mater. Sci. **50**, 925 (2011).

[73] X. Li, S. Schönecker, R. Li, X. Li, Y. Wang, J. Zhao, B. Johansson, and L. Vitos, J. Phys.: Condens. Matter **28**, 295501 (2016).